

$K\alpha$ iron line profile from accretion disks around regular and singular exotic compact objects

Cosimo Bambi* and Daniele Malafarina†

Center for Field Theory and Particle Physics & Department of Physics, Fudan University, 200433 Shanghai, China

(Dated: October 8, 2018)

The nature of the super-massive black hole candidates in galactic nuclei can be tested by analyzing the profile of the $K\alpha$ iron line observed in their X-ray spectrum. In this paper, we consider the possibility that the spacetime in the immediate vicinity of these objects may be described by some non vacuum exact solutions of Einstein’s equations resulting as the end-state of gravitational collapse. The vacuum far away portion of the spacetime is described by the Schwarzschild metric, while the interior part may be either regular or have a naked singularity at the center. The iron line generated around this class of objects has specific features, which can be used to distinguish such objects from Kerr black holes. In particular, their iron line cannot have the characteristic low-energy tail of the line generated from accretion disks around fast-rotating Kerr black holes. We can thus conclude that the super-massive black hole candidates whose spin parameter has been estimated to be close to 1 assuming the Kerr background cannot be this kind of objects.

PACS numbers: 04.20.Dw, 04.20.Jb, 98.62.Js

I. INTRODUCTION

Astrophysical black hole (BH) candidates are stellar-mass compact objects in X-ray binary systems and super-massive dark bodies at the center of every normal galaxy. They are thought to be the Kerr BH of general relativity, but their actual nature has still to be verified [1]. In fact, the only robust measurements we have so far are for the masses of these objects. In the case of stellar-mass BH candidates, the mass exceeds $3 M_{\odot}$, which is the maximum value for the mass of a neutron star for any reasonable matter equation of state [2]. Super-massive BH candidates in galactic nuclei are simply too heavy, compact, and old to be clusters of non-luminous objects, as the cluster lifetime due to evaporation and physical collisions would be shorter than the age of these systems [3]. The non-observation of electromagnetic radiation emitted by the possible surface of these objects may also be interpreted as an evidence for the existence of an event horizon [4], which is the key-feature of BHs (see however [5] and note that long-living trapped surfaces can mimic an event horizon [6]). The interpretation that astrophysical BH candidates are the Kerr BHs of general relativity is therefore the most natural explanation, and the only one that does not explicitly require new physics. However, an observational confirmation of this hypothesis would be at least desirable. Attempts to test the actual nature of these objects can be found in [7–13].

In 4-dimensional general relativity, BHs are described by the Kerr solution and they are completely specified by two parameters: the mass M and the spin angular momentum J . However, there are many solutions that are not BHs and can describe the gravitational field outside a super-massive compact object. These can vary

from non-spherical vacuum solutions with naked singularities to solutions with a non-vanishing energy momentum tensor. A super-massive compact object described by a so called “interior” solution that matches smoothly to a known vacuum exterior could in principle be an alternative explanation to the BH paradigm. In the present paper, we explore such a possibility. In [14], one of us studied the thermal spectrum of geometrically thin disks around such kind of sources, in order to determine how they would be observationally different from a BH. The non-existence of an innermost stable circular orbit (ISCO) in this class of metrics is the key-point to understand their spectrum. The radiative efficiency turns out to be very high and therefore the thermal spectrum of the disk is harder than the one around a Kerr BH with spin parameter $a_* = J/M^2 = 1$. So, the stellar-mass BH candidates in X-ray binary systems cannot be this kind of objects. In the case of the super-massive BH candidates in galactic nuclei, we cannot observe the thermal spectrum of their thin disks (the disk’s temperature is proportional to $M^{-0.25}$ and for $M \sim 10^6 - 10^9 M_{\odot}$ the spectrum is in the UV range, where dust absorption makes measurements impossible). The analysis of the $K\alpha$ iron line is currently the only available technique to probe the spacetime geometry around super-massive BH candidates. The present work is therefore devoted to the study of the iron line profile of these exotic compact objects to find observational features to test the possibility that they can be the super-massive BH candidates at the center of galaxies.

The content of the paper is as follows. In Section II, we briefly review the origin and the features of the $K\alpha$ iron line profile and its role to test the nature of BH candidates. In Section III, we introduce the interior solutions of the exotic compact objects we are going to investigate. The profiles of the $K\alpha$ iron line from this class of sources are calculated in Section IV, and we then discuss their features and their differences with the iron lines gener-

* bambi@fudan.edu.cn

† daniele@fudan.edu.cn

ated in Kerr spacetimes. Summary and conclusions are reported in Section V. Throughout the paper, we use units in which $G_N = c = 1$, unless stated otherwise.

II. $K\alpha$ IRON LINE PROFILE

The X-ray spectrum of both stellar-mass and super-massive BH candidates has often a power-law component. This feature is commonly interpreted as the inverse Compton scattering of thermal photons by electrons in a hot corona above the accretion disk. Such a “primary component” irradiates also the accretion disk, producing a “reflection component” in the X-ray spectrum. The illumination of the cold disk by the primary component also produces spectral lines by fluorescence. The strongest line is the $K\alpha$ iron line at 6.4 keV. This line is intrinsically narrow in frequency, while the one observed appears broadened and skewed. The most accepted interpretation is that the line is strongly altered by special and general relativistic effects, which produce a characteristic profile first predicted in Ref. [15] and then observed for the first time in the ASCA data of the Seyfert 1 galaxy MCG-6-30-15 [16]. For some sources, this line is extraordinarily stable, in spite of a substantial variability of the continuum, which suggests that its shape is determined by the geometry of the spacetime around the compact object rather than by the properties of the accretion flow.

The profile of the $K\alpha$ iron line depends on the metric of the spacetime, the geometry of the emitting region, the disk emissivity, and the disk’s inclination angle with respect to the line of sight of the distant observer. The background metric determines the propagation of the photons from the disk to the distant observer, the velocity of the material in the accretion disk, the gravitational redshift, and also the inner edge of the disk if the latter is supposed to be at the ISCO radius, $r_{\text{in}} = r_{\text{ISCO}}$. The geometry of the emitting regions is unknown, but the simplest option is to assume that it ranges from the inner edge r_{in} to some outer radius r_{out} . The disk emissivity is often supposed to have a power-law behavior, $I_e \propto 1/r^\alpha$, with an index α to be determined by fitting the data. The inclination of the disk with respect to the line of sight of the distant observer, say i , is usually another free parameter to be inferred during the fitting procedure. The dependence of the line profile on a_* , i , α , and r_{out} in the Kerr background has been analyzed in detail by many authors, starting with Ref. [15]. The case of iron lines generated in other spacetimes can be found in [17].

In this work, we use the code described in [17]. The photon flux number density measured by a distant observer is given by

$$\begin{aligned} N_{E_{\text{obs}}} &= \frac{1}{E_{\text{obs}}} \int I_{\text{obs}}(E_{\text{obs}}) d\Omega_{\text{obs}} = \\ &= \frac{1}{E_{\text{obs}}} \int g^3 I_e(E_e) d\Omega_{\text{obs}}. \end{aligned} \quad (1)$$

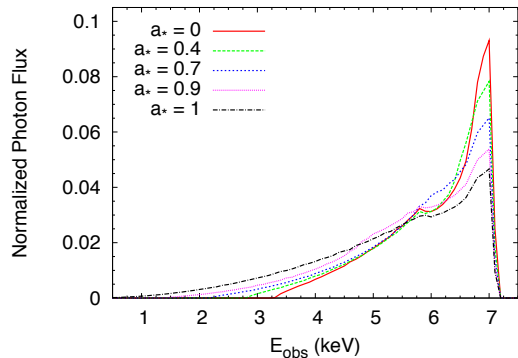


FIG. 1. Iron line profile in the Kerr background for different values of the spin parameter a_* . Model parameters: inner edge $r_{\text{in}} = r_{\text{ISCO}}$, outer edge $r_{\text{out}}/M = r_{\text{in}}/M + 100$, viewing angle $i = 45^\circ$, and index of the intensity profile $\alpha = 3$.

Here I_{obs} and E_{obs} are, respectively, the specific intensity of the radiation and the photon energy as measured by the distant observer, $d\Omega_{\text{obs}}$ is the element of the solid angle subtended by the image of the disk on the observer’s sky, I_e and E_e are, respectively, the local specific intensity of the radiation and the photon energy in the rest frame of the emitter, and $g = E_{\text{obs}}/E_e$ is the redshift factor. $I_{\text{obs}} = g^3 I_e$ follows from the Liouville’s theorem. The disk emission is assumed monochromatic with the rest frame energy $E_{K\alpha} = 6.4$ keV, and isotropic with a power-law radial profile:

$$I_e(E_e) \propto \delta(E_e - E_{K\alpha})/r^\alpha. \quad (2)$$

Doppler boosting, gravitational redshift, and frame dragging are encoded in the calculation of g , while the light bending enters in the integration. More details can be found in [17].

If we assume that astrophysical BH candidates are the Kerr BHs of general relativity, the analysis of the $K\alpha$ iron line can be used to estimate the spin parameter of these objects. Fig. 1 shows the iron line profile for different values of a_* . The key-point is the assumption that the inner edge of the disk is at the ISCO radius, which monotonically increases from $r_{\text{ISCO}}/M = 6$ for a Schwarzschild non-rotating BH to $r_{\text{ISCO}}/M = 1$ for an extremal Kerr BH with $a_* = 1$. The iron line profile of fast-rotating Kerr BHs is characterized by a low-energy tail, as a consequence of the strong gravitational redshift of the radiation emitted at small radii. Current measurements of the spin parameter of super-massive BH candidates with the analysis of the $K\alpha$ iron line (under the assumption of Kerr background) are reported in Tab. I.

III. SINGULAR AND REGULAR SPACETIMES

We shall consider here some known examples of interior solutions under the assumption of spherical symmetry for the spacetime. Therefore we will consider non-rotating interiors that match smoothly to an exterior

AGN	a_*	References
MGC-6-30-15	> 0.98	[18]
Fairall 9	0.65 ± 0.05	[19, 20]
SWIFT J2127.4+5654	0.6 ± 0.2	[21]
1H 0707-495	> 0.98	[22]
Mrk 79	0.7 ± 0.1	[23]
NGC 3783	> 0.98	[24]
Mrk 335	0.70 ± 0.12	[20]
NGC 7469	0.69 ± 0.09	[20]

TABLE I. Current measurements of the spin parameter of super-massive BH candidates with the analysis of the $K\alpha$ iron line.

Schwarzschild vacuum metric. The most general metric describing such an interior is given in Schwarzschild coordinates as

$$ds^2 = -e^{2\phi(r)} dt^2 + \frac{1}{1 - F(r)/r} dr^2 + r^2 d\Omega^2, \quad (3)$$

where $d\Omega^2$ is the line element on the unit two-sphere. The energy momentum tensor is given by

$$T = \text{diag}\{\rho, p_r, p_\theta, p_\theta\}, \quad (4)$$

where the energy density ρ and the radial and tangential pressures p_r and p_θ are functions of r that are related to the metric functions ϕ and F via Einstein's equations. The function F represents the gravitational mass contained within the radius r and from the coefficient g_{rr} in the metric (3) it is easy to see that at the boundary of the cloud r_b we have $F(r_b) = 2M$, where M is the Schwarzschild mass.

We shall assume that the cloud is transparent to radiation and it is weakly interacting with the particles in an accretion disk so that viscosity is negligible and the accretion disk can be described by circular geodesics within the cloud. This can be the case for a cloud of very low density or made of some exotic matter. Then we can study the observational properties of the accretion disk that extends within the interior solution and determine in what respect they may differ from those of accretion disks around BHs. By assuming that the particles in the accretion disk follow geodesic motion we allow in principle the disk in the inner cloud to extend all the way to the center as the ISCO for these interiors is at $r = 0$. For a realistic case on the other hand there would be an inner edge of the disk $r_{\text{in}} \neq 0$ that would be determined by the physical properties of the cloud. In fact, above certain densities, viscosity and scattering effects would deviate the particles in the disk from circular geodesic motion. Also, since the disk is emitting light, there will be a certain radius at which the radiation pressure of the light balances the gravitational attraction (Eddington luminosity) thus disrupting the accretion disk.

In the following we will consider two examples for two different kinds of interiors. Namely, we will study two interior solutions for perfect fluids and two for a cloud

sustained only by tangential pressures. In order to distinguish the most relevant physical features we chose one regular solution with constant density and one singular solution where the density diverges like r^{-2} for both fluid models.

As shown in [14], we can consider these solutions as the limit for a slowly evolving collapsing cloud. Therefore, in the singular examples the central singularity has to be interpreted as a region of arbitrarily high density where the divergence can be reached only as t goes to infinity.

The study of circular geodesics and accretion disk properties in a spherically symmetric spacetime can be done following [25]. In general, it is found that there are two different regimes of accretion depending on where the boundary is located. For $r_b < 6M$, there is a gap between the accretion disk in the Schwarzschild sector and the accretion disk in the interior. For $r_b \geq 6M$, there are stable circular orbits extending from infinity to the center. In the following we will consider always the second accretion regime.

A. Tangential pressure

Interior solutions matching to Schwarzschild and sustained only by tangential pressures ($p_r = 0$) were first studied in [26]. Einstein's equations for this case take the form

$$\rho = \frac{F'}{r^2}, \quad (5)$$

$$p_\theta = \frac{1}{2} \rho r \phi', \quad (6)$$

$$2\phi' = \frac{F(r)}{r^2 - rF(r)}, \quad (7)$$

and it is easy to see that there is the freedom to specify one free function. In the following we choose a suitable mass profile F and then determine the other quantities via Einstein's equations.

1. Regular example

To begin, we consider the constant density interior obtained by choosing

$$F = M_0 r^3. \quad (8)$$

Then Eqs. (5) and (6) give

$$\rho = 3M_0, \quad p_\theta = \frac{3M_0^2 r^2}{4(1 - M_0 r^2)}, \quad (9)$$

while from Eq. (7) written as $\phi' = \frac{M_0 r}{2(1 - M_0 r^2)}$ we get

$$e^{2\phi} = \frac{C}{\sqrt{1 - M_0 r^2}}, \quad (10)$$

with the integration constant C given by the matching condition with Schwarzschild,

$$C = -(1 - M_0 r_b^2)^{3/2}. \quad (11)$$

The metric takes the form [26]

$$ds^2 = -\frac{(1 - M_0 r_b^2)^{3/2}}{\sqrt{1 - M_0 r^2}} dt^2 + \frac{1}{1 - M_0 r^2} dr^2 + r^2 d\Omega^2, \quad (12)$$

and it is easy to see that there are no singularities in this spacetime. Furthermore the total mass for the Schwarzschild exterior is given by $2M = M_0 r_b^3$.

2. Singular example

As a second example, we consider a cloud with a singularity at the center. By choosing the free function F as

$$F = M_0 r, \quad (13)$$

from Eqs. (5) and (6) we get

$$\rho = \frac{M_0}{r^2}, \quad p_\theta = \frac{M_0}{4(1 - M_0)} \rho. \quad (14)$$

In this case, the energy density diverges as r goes to zero, and from the evaluation of the Kretschmann scalar it is easy to verify that $r = 0$ corresponds to a true curvature singularity. Note that this example corresponds to a linear equation of state $\rho = k p_\theta$, with $k = \frac{M_0}{4(1 - M_0)}$.

From Eq. (7), we get $\phi' = \frac{M_0}{2(1 - M_0)r}$, which, once integrated, gives

$$e^{2\phi} = C r^{\frac{M_0}{1 - M_0}}, \quad C = (1 - M_0) r_b^{-\frac{M_0}{1 - M_0}}, \quad (15)$$

and the metric becomes [14]

$$ds^2 = -(1 - M_0) \left(\frac{r}{r_b} \right)^{\frac{M_0}{1 - M_0}} dt^2 + \frac{1}{1 - M_0} dr^2 + r^2 d\Omega^2. \quad (16)$$

B. Perfect fluid

We now turn the attention to perfect fluid interiors that are defined by the relation between radial and tangential pressure as given by $p_r = p_\theta$. These interiors have been widely studied in the literature starting from the pioneering work by Tolman [27]. Einstein's equations take the form

$$\rho = \frac{F'}{r^2}, \quad (17)$$

$$p = \frac{2\phi'}{r} \left[1 - \frac{F(r)}{r} \right] - \frac{F(r)}{r^3}, \quad (18)$$

$$p' = -(\rho + p)\phi', \quad (19)$$

and once again the system is completely determined once we specify the mass function F . Nevertheless, in this case, solving the system of Einstein's equations is more difficult since after the choice of F we can substitute ϕ' from Eq. (18) into Eq. (19) in order to obtain the differential equation that must be satisfied by p . This is known as the Tolman-Oppenheimer-Volkoff (TOV) equation

$$p' = -(\rho + p) \frac{[pr^3 + F(r)]}{2r[r - F(r)]}, \quad (20)$$

and the system is solved once a solution for Eq. (20) is found. This is possible in some very simple special cases like the ones provided below. For a comprehensive list of known solutions for perfect fluid interiors, see for example [28].

1. Regular example

The simplest model is the constant density Schwarzschild interior with

$$F(r) = M_0 r^3. \quad (21)$$

Then again $\rho = 3M_0$ and solving the TOV equation gives the pressure

$$p = 3M_0 \frac{\sqrt{1 - M_0 r_b^2} - \sqrt{1 - M_0 r^2}}{\sqrt{1 - M_0 r^2} - 3\sqrt{1 - M_0 r_b^2}}, \quad (22)$$

which vanishes at the boundary r_b where the cloud matches the Schwarzschild exterior with total mass $M = M_0 r_b^3$. Then from Eq. (18) we get

$$e^{2\phi} = (A - \sqrt{1 - M_0 r^2})^2, \quad (23)$$

with the integration constant A given by the matching condition

$$A = 2\sqrt{1 - M_0 r_b^2}. \quad (24)$$

The metric then takes the form [29]

$$ds^2 = -(A - \sqrt{1 - M_0 r^2})^2 dt^2 + \frac{1}{1 - M_0 r^2} dr^2 + r^2 d\Omega^2. \quad (25)$$

Note that from the pressure profile we can obtain a condition for the pressure to be positive and finite at the center $p(0) > 0$. This implies the existence of a lower boundary limit $r_b^2 = \frac{8}{9M_0}$ at which the central pressure diverges. This corresponds to imposing a minimum boundary greater than the Schwarzschild radius as $r_b > \frac{9M}{4}$.

2. Singular example

As we did in the tangential pressure case, we now investigate a perfect fluid interior where the density diverges at the center. This is again given by the choice

$$F(r) = M_0 r, \quad (26)$$

for which

$$\rho = \frac{M_0}{r^2}. \quad (27)$$

To solve the TOV Eq. (20), we must define a new parameter λ as

$$\lambda = \sqrt{\frac{1 - 2M_0}{1 - M_0}}, \quad M_0 = \frac{1 - \lambda^2}{2 - \lambda^2}. \quad (28)$$

So that once we integrate the TOV equation we get the pressure as

$$p = \frac{1}{2 - \lambda^2} \frac{1}{r^2} \left(\frac{(1 - \lambda)^2 A - (1 + \lambda)^2 B r^{2\lambda}}{A - B r^{2\lambda}} \right), \quad (29)$$

where A and B are constants coming from the integration. From the integration of Eq. (18), we get

$$e^{2\phi} = (A r^{1-\lambda} - B r^{1+\lambda})^2. \quad (30)$$

The two integration constants A and B are determined by the matching condition for g_{tt} and by the condition that p must vanish at the boundary. They can be written as

$$A = \frac{(1 + \lambda)^2 r_b^{\lambda-1}}{4\lambda\sqrt{2 - \lambda^2}}, \quad (31)$$

$$B = \frac{(1 - \lambda)^2 r_b^{-\lambda-1}}{4\lambda\sqrt{2 - \lambda^2}}, \quad (32)$$

and the metric takes the form [14]

$$ds^2 = -(A r^{1-\lambda} - B r^{1+\lambda})^2 dt^2 + (2 - \lambda^2) dr^2 + r^2 d\Omega^2. \quad (33)$$

Note that in this case the relation between ρ and p is more complicated than in the corresponding tangential pressure case, but it tends to a stiff fluid equation of state $\rho = p$ in the limit $\lambda = 0$ (which corresponds to $M_0 = 1/2$) and thus implies a minimum boundary radius of $r_b = 4M$, greater than the one obtained for the regular example above.

IV. RESULTS AND DISCUSSION

We can now use the solutions presented in the previous section to compute the associated $K\alpha$ iron line. The free parameters of the model are: the radius of the compact object, r_b , the inner and outer edges of the accretion disk, r_{in} and r_{out} , the disk's inclination angle with respect to the line of sight of the distant observer, i , and the index of the intensity profile, α . The dependence of the iron line on r_{out} , i , and α is the same of the one in the Kerr geometry and it is already well studied in the literature. So, in what follows we will always consider the specific case with $r_{\text{out}} = r_{\text{in}} + 100 M$, $i = 45^\circ$, and $\alpha = 3$. We will thus focus our attention on the effects of r_b and r_{in} .

In the Kerr background, r_{in} is supposed to be the ISCO radius. For the interior solutions described in the previous section, there is no ISCO radius, in the sense that circular orbits are always stable. The reason is that gravity is never so strong to make the orbit unstable, and this is due to the fact that the mass of the objects is not concentrated at $r = 0$, and the total mass inside the sphere of radius r decreases as r decreases. As said, the choice $r_{\text{in}} = 0$ is likely not very physical, because the density of the disk at small radii would diverge, with the result that the thin disk approximation would break down. We can assume r_{in} a free parameter, but we will see that our conclusions are not sensitive to the exact choice of r_{in} . As $r_{\text{ISCO}} = 6 M$ in the Schwarzschild background, to prevent the formation of two disconnected disks with strange features (see the discussion in the previous section and, for more details, the one in Ref. [14]), we will assume that the physical radius of the compact object is $r_b \geq 6 M$.

Let us start considering the singular tangential pressure case. If we set $r_{\text{in}} = r_b = 6 M$, we find an iron line very similar to the one from a Schwarzschild BH. The small difference is due to the fact that around a Schwarzschild BH some photons may cross the photon capture sphere and be swallowed by the BH (the effect is larger for edge-on disks). If we reduce the value of r_{in} without changing the one of r_b , we get the profiles shown in the left panel of Fig. 2. On the other hand, if we increase the value of r_b maintaining $r_{\text{in}} = 6 M$, we find the profiles in the right panel of Fig. 2. The resulting iron line for small values of r_{in} can be better understood if we compare it with the iron line generated around an extremal Kerr BH, paying attention to the contribution from different radii. This is done in Fig. 3. In both the models, $r_{\text{in}} = M$. There are clearly some important dif-

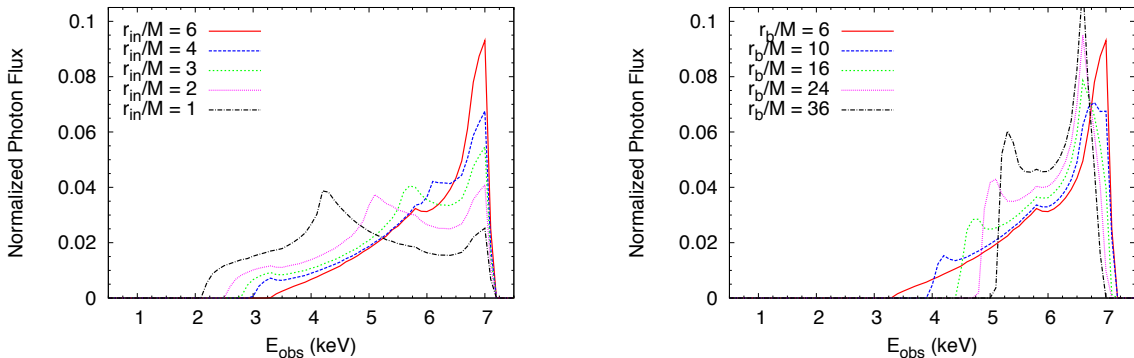


FIG. 2. Iron line profile in the singular tangential pressure case. Left panel: $r_b/M = 6$ and $r_{in}/M = 6, 4, 3, 2,$ and 1 . Right panel: $r_{in}/M = 6$ and $r_b/M = 6, 10, 16, 24,$ and 36 . The outer edge is set at $r_{out}/M = r_{in}/M + 100$, the viewing angle is $i = 45^\circ$, and the index of the intensity profile is $\alpha = 3$.

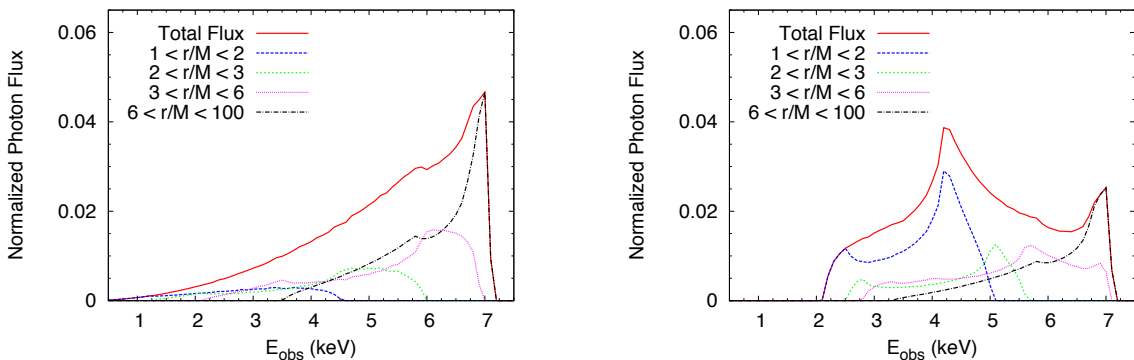


FIG. 3. Iron line profile in the case of Kerr background with $a_* = 1$ (left panel) and singular tangential pressure metric (right panel). In both examples, the inner edge of the disk is supposed at the radial coordinate $r_{in}/M = 1$, the outer edge is set at $r_{out}/M = 100$, the viewing angle is $i = 45^\circ$, and the index of the intensity profile is $\alpha = 3$. The panels show the total flux as well as the corresponding contributions from the disk regions $1 < r/M < 2$, $2 < r/M < 3$, $3 < r/M < 6$, and $6 < r/M < 100$.

ferences. First, there are many photons coming from the region $1 < r/M < 2$ of the exotic compact object, while the photon contribution from the same region is very low in the Kerr BH case. In the former case, the contribution is important because the intensity goes like $1/r^3$. However, in the BH case many photons emitted from the region close to the compact object cannot reach the distant observer because swallowed by the BH. In other words, the effect of light bending at small radii is quite different in the two backgrounds. Second, a remarkable difference between the two iron line profiles is the low-energy tail. In the case of the extremal BH, the photons coming from the region at small radii are strongly gravitational redshifted. This is simply the result of the presence of the event horizon – at the event horizon, the gravitational redshift is zero. In the case of the exotic compact object, there is no event horizon and therefore the gravitational redshift is much weaker. At large radii, $6 < r/M < 100$, the two models have roughly the same line (the difference in the left and right panels is just the normalization, but the shape is practically the same). The difference in the iron line profiles shown in the right panel of Fig. 2 is

mainly due to the different gravitational redshift and to the different angular velocity of the accreting gas. The latter is smaller in the case of exotic compact object, so the Doppler redshift and blueshift are milder. For instance, the characteristic peak at high energies in the profile is due to the Doppler blueshift at relatively large radii ($r/M \sim 10$), where the gravitational redshift is subdominant. When $r_b/M \gtrsim 10$, the peak moves to lower energies.

We can now repeat the calculations for the other interior solutions. The qualitative features of the new iron line profiles are more or less the same as the singular tangential pressure case. Fig. 4 shows the regular tangential pressure scenario. We can find the same characteristic features. The gravitational redshift is not as important as in the BH background even when the inner edge of the disk is at small radii. The effect of light bending is also an important difference with the BH case, and photons emitted at small radii can easily reach the distant observer, with the clear result that their contribution in the line profile is quite significant. The angular frequency of the gas in the accretion disk is lower than the one around

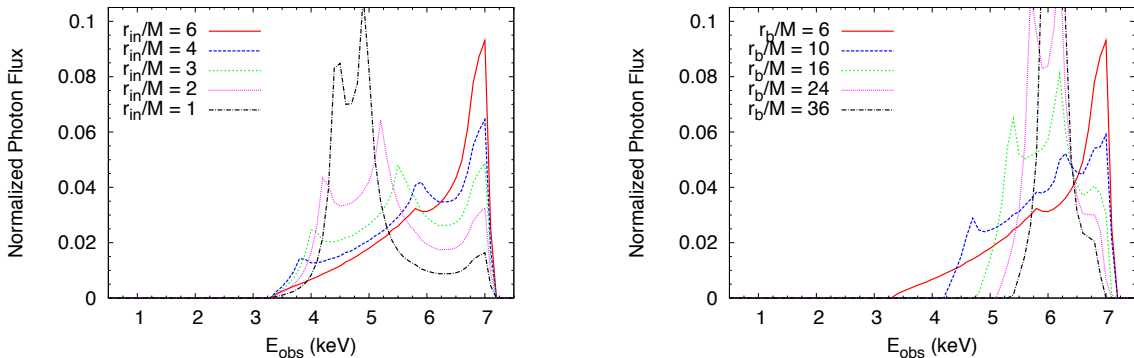


FIG. 4. As in Fig. 2 for the regular tangential pressure metric.

a BH, so the Doppler redshift and blueshift are milder. The iron lines of the perfect fluid solutions are reported in Figs. 5 (singular case) and 6 (regular case).

V. SUMMARY AND CONCLUSIONS

The super-massive objects at the center of galaxies are thought to be the Kerr BHs of general relativity, but their actual nature has still to be verified. In the present paper, we have explored the possibility that these objects are instead exotic compact bodies described by a so called “interior” solution that smoothly matches to a known vacuum exterior, and we have looked for possible observational signatures to observationally distinguish this class of objects from Kerr BHs. Today, the only available technique to probe the spacetime geometry around super-massive BH candidates is the analysis of the $K\alpha$ iron line. We have thus calculated the iron lines that can be generated in these spacetimes and then compared with the ones of Kerr BHs. It turns out that the profiles of the iron line of this class of exotic objects have some specific observational signatures. In particular:

1. Despite that the inner edge of the accretion disk can be at much smaller radii than the one of the disk around a Kerr BH (a key-feature of these solutions is the absence of a finite ISCO radius), the iron line cannot have the characteristic low-energy tail expected for the line of a fast-rotating BH. These is a consequence of the mild gravitational redshift.
2. Photons emitted by the inner part of the accretion disk, close to the compact object, can more easily escape to infinity and reach the distant observer. The contribution of the radiation emitted at small radii is thus significant, with the effect of producing a peak in the profile absent in the BH case. Photons emitted at small radii around a Kerr BH are instead easily captured by the latter, so their contribution to the total photon flux detected at infinity is small.

3. If the physical radius of the compact object r_b exceeds 10 – 15 gravitational radii, the maximum Doppler blueshift is reduced, so the high energy peak in the iron line profile moves to lower energies with respect to the BH case.

The general features described above are common to all the four “interiors” studied here and we can argue that they are most likely common to any reasonable interior model. Therefore even if here we have only considered some *ad hoc* cases of non-rotating objects, we stress that our conclusions are likely to remain true even in the more realistic case of rotating bodies. In the BH case, the spin of the compact object simply moves the inner edge of the disk to smaller radii, so that the line of fast-rotating Kerr BHs is characterized by a low-energy tail due to the strong gravitational redshift at small radii. In the case of our exotic compact objects, there is no ISCO and therefore a non-vanishing rotation only introduces small corrections in the photon propagation and in the angular velocity of the gas in the accretion disk. We thus expect that the associated iron line is quite similar to the one of the non-rotating case computed in this work.

In conclusion, the $K\alpha$ iron line of the class of exotic objects considered in this paper has specific features to be observationally distinguished from the one associated to a Kerr BH. The few super-massive BH candidates whose iron line has been analyzed in detail in the literature do not have an iron line with these features and therefore we can exclude the possibility that they are the ‘interior’ solutions studied in this paper. However, we are talking about 6 sources (see Tab. I), while the super-massive BH candidates in the visible Universe should be around 10^{12} , and it is not impossible that some of them are exotic compact bodies whose nature differs significantly from that of BHs. Therefore the possibility remains that some of these candidates can be described by an interior solution similar to the ones presented here, either regular or singular.

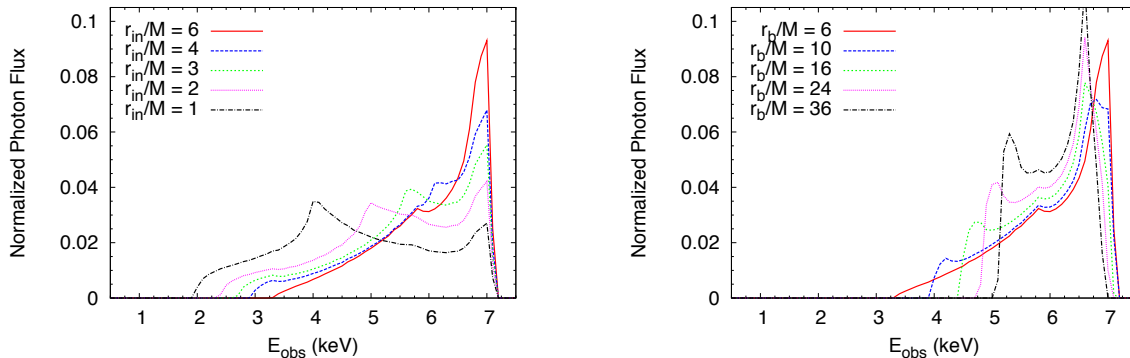


FIG. 5. As in Fig. 2 for the singular perfect fluid metric.

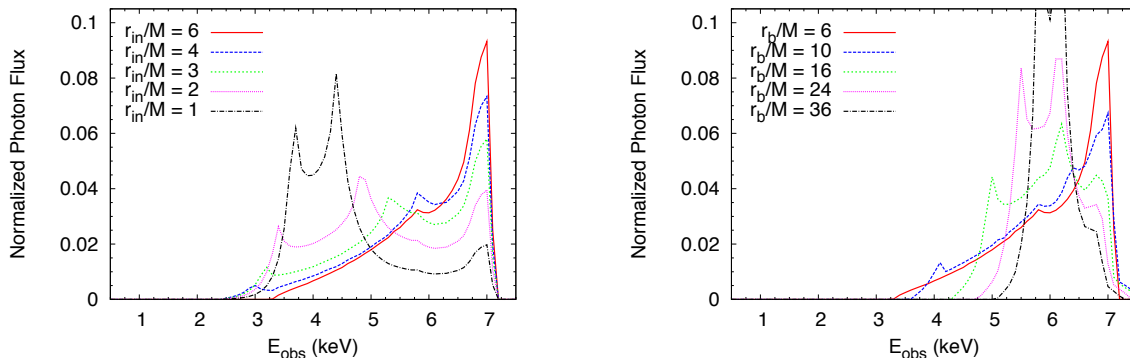


FIG. 6. As in Fig. 2 for the regular perfect fluid metric.

ACKNOWLEDGMENTS

This work was supported by the Thousand Young Talents Program and Fudan University.

-
- [1] R. Narayan, *New J. Phys.* **7**, 199 (2005) [gr-qc/0506078]; C. Bambi, *Mod. Phys. Lett. A* **26**, 2453 (2011) [arXiv:1109.4256 [gr-qc]]; C. Bambi, *Astron. Rev.* **8**, 4 (2013) [arXiv:1301.0361 [gr-qc]].
- [2] C. E. Rhoades and R. Ruffini, *Phys. Rev. Lett.* **32**, 324 (1974); V. Kalogera and G. Baym, *Astrophys. J.* **470**, L61 (1996).
- [3] E. Maoz, *Astrophys. J.* **494**, L181 (1998) [astro-ph/9710309].
- [4] J. E. McClintock, R. Narayan and G. B. Rybicki, *Astrophys. J.* **615**, 402 (2004) [astro-ph/0403251]; R. A. Remillard, D. Lin, R. L. Cooper and R. Narayan, *Astrophys. J.* **646**, 407 (2006) [astro-ph/0509758]; R. Narayan and J. E. McClintock, *New Astron. Rev.* **51**, 733 (2008) [arXiv:0803.0322 [astro-ph]]; A. E. Broderick, A. Loeb and R. Narayan, *Astrophys. J.* **701**, 1357 (2009) [arXiv:0903.1105 [astro-ph.HE]].
- [5] M. A. Abramowicz, W. Kluzniak and J. -P. Lasota, *Astron. Astrophys.* **396**, L31 (2002) [astro-ph/0207270]; C. Bambi, *The Scientific World Journal* **2013**, 204315 (2013) [arXiv:1205.4640 [gr-qc]].
- [6] C. Bambi, D. Malafarina and L. Modesto, *Phys. Rev. D* **88**, 044009 (2013) arXiv:1306.1668 [gr-qc].
- [7] C. Bambi, *Europhys. Lett.* **94**, 50002 (2011); *Phys. Rev. D* **83**, 103003 (2011); *JCAP* **1105**, 009 (2011); *Phys. Lett. B* **705**, 5 (2011); *Phys. Rev. D* **85**, 043001 (2012); *Phys. Rev. D* **85**, 043002 (2012); *Phys. Rev. D* **86**, 123013 (2012); *JCAP* **1209**, 014 (2012); *Astrophys. J.* **761**, 174 (2012); *Phys. Rev. D* **87**, 107501 (2013); *JCAP* (in press) [arXiv:1305.5409 [gr-qc]].
- [8] C. Bambi and K. Freese, *Phys. Rev. D* **79**, 043002 (2009); C. Bambi and N. Yoshida, *Class. Quant. Grav.* **27**, 205006 (2010); C. Bambi and E. Barausse, *Astrophys. J.* **731**, 121 (2011); C. Bambi and L. Modesto, *Phys. Lett. B* **706**, 13 (2011); C. Bambi, F. Caravelli and L. Modesto, *Phys. Lett. B* **711**, 10 (2012); Z. Li and C. Bambi, *JCAP* **1303**, 031 (2013); C. Bambi and G. Lukes-Gerakopoulos, *Phys. Rev. D* **87**, 083006 (2013).
- [9] C. Bambi, K. Freese, T. Harada, R. Takahashi and N. Yoshida, *Phys. Rev. D* **80**, 104023 (2009) [arXiv:0910.1634 [gr-qc]]; C. Bambi, T. Harada, R. Takahashi and N. Yoshida, *Phys. Rev. D* **81**, 104004 (2010)

- [arXiv:1003.4821 [gr-qc]].
- [10] D. F. Torres, Nucl. Phys. B **626**, 377 (2002) [hep-ph/0201154]; Y. Lu and D. F. Torres, Int. J. Mod. Phys. D **12**, 63 (2003) [astro-ph/0205418].
- [11] T. Harko, Z. Kovacs and F. S. N. Lobo, Phys. Rev. D **78**, 084005 (2008) [arXiv:0808.3306 [gr-qc]]; Phys. Rev. D **80**, 044021 (2009) [arXiv:0907.1449 [gr-qc]]; Class. Quant. Grav. **27**, 105010 (2010) [arXiv:0909.1267 [gr-qc]].
- [12] T. Johannsen and D. Psaltis, Astrophys. J. **716**, 187 (2010) [arXiv:1003.3415 [astro-ph.HE]]; Astrophys. J. **718**, 446 (2010) [arXiv:1005.1931 [astro-ph.HE]]; Astrophys. J. **726**, 11 (2011) [arXiv:1010.1000 [astro-ph.HE]]; Phys. Rev. D **83**, 124015 (2011) [arXiv:1105.3191 [gr-qc]].
- [13] N. Wex and S. Kopeikin, Astrophys. J. **514**, 388 (1999) [astro-ph/9811052]; K. Glampedakis and S. Babak, Class. Quant. Grav. **23**, 4167 (2006) [arXiv:gr-qc/0510057]; L. Barack and C. Cutler, Phys. Rev. D **75**, 042003 (2007) [arXiv:gr-qc/0612029]; H. Krawczynski, Astrophys. J. **754**, 133 (2012) [arXiv:1205.7063 [gr-qc]].
- [14] P. S. Joshi, D. Malafarina and R. Narayan, Class. Quant. Grav. **28**, 235018 (2011) [arXiv:1106.5438 [gr-qc]]; P. S. Joshi, D. Malafarina and R. Narayan, arXiv:1304.7331 [gr-qc].
- [15] A. C. Fabian, M. J. Rees, L. Stella and N. E. White, Mon. Not. Roy. Astron. Soc. **238**, 729 (1989).
- [16] Y. Tanaka, K. Nandra, A. C. Fabian, H. Inoue, C. Otani, T. Dotani, K. Hayashida and K. Iwasawa *et al.*, Nature **375**, 659 (1995).
- [17] C. Bambi, Phys. Rev. D **87**, 023007 (2013) [arXiv:1211.2513 [gr-qc]]; Phys. Rev. D **87**, 084039 (2013) [arXiv:1303.0624 [gr-qc]].
- [18] L. W. Brenneman and C. S. Reynolds, Astrophys. J. **652**, 1028 (2006) [astro-ph/0608502].
- [19] S. Schmoll, J. M. Miller, M. Volonteri, E. Cackett, C. S. Reynolds, A. C. Fabian, L. W. Brenneman and G. Miniutti *et al.*, Astrophys. J. **703**, 2171 (2009) [arXiv:0908.0013 [astro-ph.HE]].
- [20] A. R. Patrick, J. N. Reeves, D. Porquet, A. G. Markowitz, A. P. Lobban and Y. Terashima, Mon. Not. Roy. Astron. Soc. **411**, 2353 (2011) [arXiv:1010.2080 [astro-ph.HE]].
- [21] G. Miniutti, F. Panessa, A. De Rosa, A. C. Fabian, A. Malizia, M. Molina, J. M. Miller and S. Vaughan, Mon. Not. Roy. Astron. Soc. **398**, 255 (2009) [arXiv:0905.2891 [astro-ph.HE]].
- [22] A. C. Fabian, A. Zoghbi, R. R. Ross, P. Uttley, L. C. Gallo, W. N. Brandt, A. Blustin and T. Boller *et al.*, Nature **459**, 540 (2009) [arXiv:0905.4383 [astro-ph.HE]].
- [23] L. C. Gallo, G. Miniutti, J. M. Miller, L. W. Brenneman, A. C. Fabian, M. Guainazzi and C. S. Reynolds, Mon. Not. Roy. Astron. Soc. **411**, 607 (2011) [arXiv:1009.2987 [astro-ph.HE]].
- [24] L. W. Brenneman, C. S. Reynolds, M. A. Nowak, R. C. Reis, M. Trippe, A. C. Fabian, K. Iwasawa and J. C. Lee *et al.*, Astrophys. J. **736**, 103 (2011) [arXiv:1104.1172 [astro-ph.HE]].
- [25] D. Novikov and K. S. Thorne in Black Holes, ed. C. DeWitt and B. S. DeWitt, New York: Gordon and Breach, p. 343 (1973); D. N. Page and K. S. Thorne, Astrophys. J. **191**, 499 (1974).
- [26] P. S. Florides, Proc. Roy. Soc. (London) Ser. A **337**, 529 (1974).
- [27] R. C. Tolman, Phys. Rev. **55**, 364 (1939).
- [28] M. S. R. Delgaty and K. Lake, Comput. Phys. Commun. **115**, 395 (1998).
- [29] H. A. Buchdahl, Phys. Rev. **116**, 1027 (1959).